Design and parametrization analysis of a reduced-order electrochemical model of graphite/LiFePO$_4$ cells for SOC/SOH estimation

James Marcicki [a,b,]*, Marcello Canova [a], A. Terrence Conlisk [a], Giorgio Rizzoni [a]

[a] Center for Automotive Research, The Ohio State University, 930 Kinnear Rd., Columbus, OH 43212, USA
[b] Research and Innovation Center, Ford Motor Company, 2101 Village Rd., Dearborn, MI 48124, USA

HIGHLIGHTS

► An improvement of the "single particle" model that includes concentration and potential dynamics of the liquid phase.
► A frequency-based, order reduction technique produces a parametric low order model.
► A novel identification process defines the model parameter temperature dependence.
► Experimental data validates the model for automotive operating conditions.

ARTICLE INFO

ABSTRACT

The design of predictive, electrochemical, Li-ion battery models and the use of model-order reduction techniques to extract low-order models enables researchers to address problems related to model-based control, estimation, aging, and life-cycle prediction. This paper presents a novel approach to the design and parametrization of a reduced-order model characterizing the dynamic voltage response of a Li-ion cell. The model is based on the assumption of uniform active material utilization and includes prediction of the ionic concentration and potential dynamics in the liquid phase, which significantly affects the voltage response for high currents. A model-order reduction procedure based on the Pade approximation method is used to reduce the partial differential equation model to a low-order system of ordinary differential equations. Systematic methods are proposed to identify the electrochemical parameters that govern power and capacity prediction, as well as their temperature dependence. The procedure is based on carefully designed experiments that isolate the influence of small groups of parameters on the voltage output, utilizing complete cell data for model identification almost entirely in place of half-cell characterization. Finally, an extensive validation with experimental data illustrates the ability of the model to accurately predict the cell voltage.

1. Introduction

Lithium-ion (Li-ion) batteries are a key technology for enabling the electrification of the automobile, due to their improved energy and power density, and potential cost savings compared to previous battery chemistries [1–3]. Automotive manufacturers have shown interest in using Li-ion batteries in the incoming generation of hybrid (HEV), plug-in hybrid (PHEV), and pure electric (EV) vehicles.

Considerable efforts are directed to modeling Li-ion battery performance, specifically predicting the output voltage in response to current and ambient temperature input conditions. This is particularly important for predicting the fuel economy and performance of electrified vehicles for different usage scenarios. Several modeling approaches have been developed to support such tasks, ranging from first-principle models based on nonlinear coupled partial differential equation (PDE) to equivalent-circuit models solved as low-order systems of ordinary differential equations (ODEs).

Equivalent circuits are characterized by low computational complexity due to their use of systems of linear or nonlinear ODEs,

* Corresponding author. Research and Innovation Center, Ford Motor Company, 2101 Village Rd., Dearborn, MI 48124, USA. Tel.: +1 734 968 9589; fax: +1 614 292 3244.
E-mail addresses: marcicki.1@osu.edu (J. Marcicki), canova.1@osu.edu (M. Canova), conlisk.1@osu.edu (A.T. Conlisk), rizzoni.1@osu.edu (G. Rizzoni).

and can be designed to implement systematic parameterization methods [4—9]. However, they generally do not provide insight into the physical and chemical phenomena driving the voltage dynamics of the cell, unless great care is taken to associate the equivalent circuit parameters with specific electrochemical processes. In this case, much of the benefit of using an equivalent circuit is forfeited because the model becomes overly complex and more difficult to parameterize as additional resistance or capacitance elements are added.

Conversely, porous electrode theory [10,11] has enabled the design of numerous first-principles battery electrochemical models. These models generally combine a description of the mass transport phenomena within the cell through the use of diffusion PDEs, with sets of nonlinear algebraic equations describing the relationships between the concentration of ions in the solid and liquid phase and the local current density. Such models match experimental data well with a limited number of calibration parameters while furnishing a wealth of information about internal electrochemical processes. Since the parameters of electrochemical models have physical meaning, being associated to mass, charge, and energy conservation principles, calibration techniques based on half-cell measurements or material characterization data are possible. On the other hand, the numerical complexity of porous electrode models is significant, which presents difficulties when applying them to real-time estimation or control, large scale simulations such as cycle-life prediction for a multitude of operating points, or system-level electrified vehicle usage studies.

For these reasons, attempts at reducing the complexity of electrochemical models have been recently made through the application of model-order reduction (MOR) techniques. Most contributions focus on reducing the simulation time of electrochemical models by reducing the order and dimensionality of the equations describing the mass diffusion in the solid phase of the electrodes. The polynomial approximation is a common technique [12—14], as well as the finite volume discretization [15], and the Pade approximation methods [16]. Proper orthogonal decomposition has also been applied as a MOR approach [17,18], and semi-analytical solutions have been presented, in some cases allowing for a variable diffusion coefficient in the solid phase [19].

Other research has focused on model reformulation [20—24] or obtaining an impedance-based model through residue grouping [25,26]. These methods are excellent for creating a reduced order model for battery performance at the beginning of battery life and allow one to deduce a model that is simple enough for parameter [27] or state-of-charge (SOC) [28] estimation. A numerical set of eigenvalues is generated for a particular model and parameter set, but as the battery parameters change due to aging, such as reduced electrode porosity or loss of active material, it is difficult to interpret how the eigenvalues will respond. This limits the applicability of these methods for real-time, long term life estimation with moderate to severe levels of battery power or energy degradation.

Most of the above methods pose several limits in their application, as they either require a priori knowledge of the system inputs, or still involve the solution of nonlinear, coupled ODEs. Furthermore, most applications of MOR methods to electrochemical models (for instance, see Ref. [13,16]) focus on simplifying the porous electrode PDEs for reducing the computational burden. In this sense, there is considerable interest today in the application of MOR techniques to extract extremely low-order battery cell models oriented to model-based control or estimation, particularly in relation with aging and life-cycle prediction.

As another potential option several authors have designed simplified electrochemical models that solve only a representative solid diffusion problem within each electrode [29]. This approach, while still retaining physically meaningful variables, eliminates the multi-scale coupling between the diffusion PDEs in the different cell domains by neglecting the spatial dependence of the intercalation current density. Eliminating the coupling between the potential and diffusion equations considerably reduces the computational requirements, as only two decoupled PDEs have to be solved. Model-order reduction methods can then be applied to further reduce the mathematical formulation of the model to a low-order set of ordinary differential equations and algebraic expressions describing the battery terminal voltage, of comparable complexity to an equivalent circuit model. Due to the reduction in complexity, this model structure is attractive from a systems perspective for control, estimation, or prognostics applications [30—33]. Cycling results for this model have been presented alongside porous electrode and polynomial approximation models [13] to illustrate their utility for low current rates. However, the formulation of the so-called single particle model either neglects the liquid phase overpotential or approximates it as a purely resistive phenomenon, thus neglecting concentration gradients in the liquid phase. Retaining some representation of the liquid phase diffusion dynamics is the ideal solution since these dynamics can become a limiting factor during high rates of discharge prevalent in HEV operation. Recent work has accounted for relaxation gradients in the liquid phase by empirically fitting relaxation data to an ODE-based model [34] that resulted from a modal transform approach and used the model for state-of-health (SOH) estimation [35]. However, the liquid phase model of Ref. [34] is still not parametric in the sense that it is not obtained from physically measurable parameters such as the salt diffusion coefficient, component porosities, or component thicknesses.

In addition to designing a model structure that is amenable for control and estimation, another practical issue with the implementation of electrochemical models is parametrization. Electrode and electrolyte properties must be characterized for the intended temperature range. While most of such properties are available to cell manufacturers, they are difficult to access for battery end-users, which reduces opportunities for incorporating accurate and robust electrochemical models into the design process for advanced battery management systems.

In this paper, a novel modeling approach bridges the gap between the complex multiscale models based on porous electrode theory and the models based on the single particle approximation. The objective of this study is to develop a reduced-order electrochemical model for Li-ion battery cells that has a mathematical structure amenable for estimation and control purposes, namely as a low-order system of linear ODEs. The model should accurately predict the cell output voltage dynamics in a broad range of C-rate conditions and retain a parametric dependence on electrochemical quantities that are measurable. The proposed model invokes a set of assumptions that allow for decoupling the PDEs describing the lithium ion diffusion dynamics in the solid and liquid phase, and takes advantage of a formal model-order reduction procedure based on Pade approximation.

The model is identified with a systematic procedure that utilizes experimental data which exercises only a subset of the system dynamics. Each phase of parametrization incorporates previously identified parameters to reduce the number of unknown values being identified by each procedure and to ensure that the identified values retain their physical interpretation. Finally, the model is extensively validated via comparison with current profiles ranging from constant current pulses to the United States Department of Energy PHEV charge depleting (CD) profile [36], each for operating temperatures ranging from 5 °C to 55 °C.

2. Experimental setup

In this study, a cylindrical cell of diameter 26 mm and height of 65 mm (26,650) is considered with nominal capacity of 2.3 Ah and nominal voltage of 3.3 V. The cell electrolyte is assumed to be 1.0 M $LiPF_6$ in a 1:1 mixture of EC:DMC, and the negative/positive electrode couple is Li_zC_6/Li_yFePO_4. The relevant internal geometric dimensions of the cell are summarized in Table 1. With the exception of the negative active particle radius, which is fixed to a typical literature value, each of these measurements were obtained from microscopy imaging techniques or basic measurements performed on a disassembled cell.

The cell terminal voltage, current, and temperature are recorded using a sample frequency of 10 Hz. Current commands are controlled at a frequency of 100 Hz using a Kepco load and Lambda supply with a Labview interface to a standard PC. Thermoelectric temperature control is achieved using a Peltier junction that is in direct contact with the aluminum cell fixture.

3. Model development

Fig. 1 provides a schematic description of the model considered in this study, showing the solid and liquid phase computation domains. The proposed model structure stems from the single particle principle [29], with the introduction of two novel extensions. First, a time-varying resistance that accounts for the resistive reactant nature of the Li_yFePO_4 electrode [37] is included. Second, the concentration overpotential from the liquid phase is modeled by applying the assumption of uniform intercalation current density to generate a solution for the liquid diffusion PDE. While the time-varying resistance is specific to systems with low solid phase electronic conductivity, the liquid phase model is applicable to all porous Li-ion electrodes.

The model description begins with the definition of the cell output voltage $V(t)$, which results from subtracting the overpotential arising from several electrochemical phenomena from the time-varying open circuit voltage (OCV)

$$V(t) = \left(U_p(t) - U_n(t)\right) - \left(\phi_e(L_c, t) - \phi_e(0, t)\right) - \left(\eta_p(t) - \eta_n(t)\right)$$
$$- (R_r(t) + R_c)I(t) - V_h(t) \tag{1}$$

The functional form of the OCV for Li_zC_6 ($U_n(t)$) and Li_yFePO_4 ($U_p(t)$) is reported in Ref. [38,39] for the cell considered in this work. As discussed in Ref. [40], a significant path dependence of the OCV for both Li_yFePO_4 and Li_zC_6 has been observed, leading to hysteresis. This phenomenon is modeled as a first order system with gain H and hysteresis transition factor τ_h [4]

$$\frac{dV_h}{dt} = |I|\tau_h(T)(H(T, SOC) - V_h) \tag{2}$$

Upon inspection, if the current is zero, the hysteresis voltage does not change. As explained in Ref. [40] there are actually some
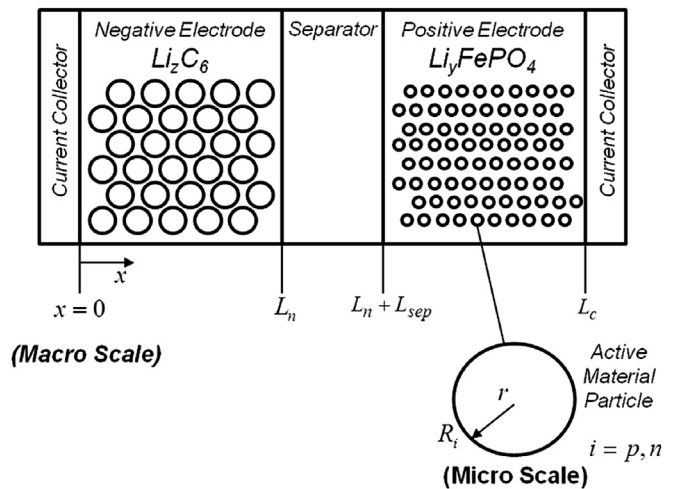
relaxation phenomena that may be a result of hysteresis that occur on the time scale of seconds following the interruption of current, but Eq. (2) models only the hysteresis effect that remains after large duration rest periods.

Deviations from the thermodynamic OCV when passing current may be attributed to ohmic, kinetic, and concentration overpotential, where each can occur in the solid or liquid phase. While the ohmic overpotential may be neglected in the negative electrode due to the high conductivity of Li_zC_6 (≈ 100 S m^{-1}), it is a significant loss in the positive electrode. Though the exact source of increasing ohmic resistance with respect to depth of discharge is unknown, a likely explanation is the Li_yFePO_4 electrode selectively charging or depleting the active material in an ohmically dominated fashion, such that the current density moves from areas with higher conductivity to lower.

Some authors have proposed that the current density moves through the electrode thickness from the current collector to the separator [41]. Others have suggested that the local current density shifts from particles with low electronic contact resistance to the conductive carbon coating to those with higher contact resistance as low-resistance sites are depleted [38]. The same phenomena has also been interpreted as a current density that is non-uniform along the particle surface in the polar and asimuth coordinates, which in theory requires a three-dimensional solution though the authors retained the one-dimensional spherical model [37].

The first approach requires the solution of the fully coupled set of porous electrode PDEs. A particle size distribution is required for the second approach, which may add a prohibitive number of model states while also requiring an iterative procedure to solve. Each of these aspects is undesirable for control or estimation applications. To avoid these difficulties, the resistive reactant effect is conceptualized here as a pure integrator, causing an increasing resistance with respect to depth-of-discharge during a current pulse response.

$$R_r(t) = \frac{R_p L_{cond}(t)}{3 L_p A \varepsilon_p} \frac{1}{\sigma_p} \tag{3}$$

The conduction length $L_{cond}(t)$ is computed by considering the path for current along a spherical active material particle. If current needed to travel along the entire half-circumference of an active material particle to reach the conductive matrix, then the total

Fig. 1. Schematic of unit cell idealized geometry with solid (r) and liquid (x) diffusion domains.

Table 1
Cell internal physical dimensions.

Parameter	Definition	Value
L_n	Negative electrode thickness	50×10^{-6} m
L_{sep}	Separator thickness	25×10^{-6} m
L_p	Positive electrode thickness	98×10^{-6} m
R_n	Negative active particle radius	3.5×10^{-6} m
R_p	Positive active particle radius	50×10^{-9} m
A	Current collector area	1.9×10^{-1} m^2

conduction length would be πR_p. Thus the actual conduction length increases in time at a rate proportional to the current according to

$$\frac{dL_{\text{cond}}}{dt} = \frac{\pi R_p |I|}{Fc_{\text{max},p}L_p A \varepsilon_p} \tag{4}$$

The ohmic loss from this resistance is referred to as the resistive reactant or time-varying ohmic overpotential. It is added to a similar loss arising from the contact resistance R_c, also referred to as the initial ohmic overpotential, as shown in Eq. (1).

Concentration overpotential in the solid phase occurs due to the limited ability of lithium ions to diffuse through the active material. This phenomenon is modeled by solving the mass diffusion equation describing transport within a representative spherical particle of active material

$$\frac{\partial c_i}{\partial t} = \frac{D_i}{r^2}\frac{\partial}{\partial r}\left(r^2\frac{\partial c_i}{\partial r}\right) \tag{5}$$

where $i = p, n$ to specify the positive or the negative electrode. The imposed boundary conditions are:

$$\left.\frac{\partial c_i}{\partial r}\right|_{r=0} = 0, \quad D_i\left.\frac{\partial c_i}{\partial r}\right|_{r=R_i} = -\frac{j_i(t)}{F} \tag{6}$$

representing symmetry at the center of the particle and a prescribed flux at the particle surface. The surface value of lithium concentration, $c_i(R_i,t)$ governs many facets of the electrochemical behavior of the cell. For instance, concentration overpotential results from the variation between the mean concentration and the surface value.

The kinetic overpotential is governed by the Butler–Volmer law. The intercalation current density $j_i(x,t)$ has been assumed constant with respect to the direction x along the unit cell thickness

$$j_i(x,t) = j_i(t) = \frac{I(t)}{a_i AL_i} \tag{7}$$

where AL_i denotes the electrode volume, a_i is the surface area per unit volume defined as $3\varepsilon_i/R_i$, and ε_i is the active material volume fraction of the electrode. Inverting the Butler–Volmer law leads to the expression for the kinetic overpotential

$$\eta_i = \frac{\overline{R}T}{\alpha F}\sinh^{-1}\left(\frac{j_i(t)}{2i_{0,i}}\right) \tag{8}$$

with the exchange current density $i_{0,i}$ defined as:

$$i_{0,i} = Fk_i\sqrt{c_i(R_i)c_{e,i}(c_{\text{max},i} - c_i(R_i))} \tag{9}$$

Increased values of the kinetic rate constants k_i will lead to decreased kinetic overpotential. As the surface concentration c_i approaches the saturation value $c_{\text{max},i}$, or tends to zero, the kinetic overpotential increases.

The liquid phase contains ohmic and concentration sources of overpotential [42]. The governing equation of transport within the liquid is given by

$$\varepsilon_e\frac{\partial c_e}{\partial t} = D_e\frac{\partial^2 c_e}{\partial x^2} + \frac{a_i(1 - t_0^+)}{F}j_i(t) \tag{10}$$

where under the assumptions introduced by Eq. (7) the intercalation current $j_i(t)$ is assumed as piecewise constant in the positive and negative electrode, and zero in the separator region. The imposed boundary conditions at each end of the unit cell are

$$\left.\frac{\partial c_e}{\partial x}\right|_{x=0,L_c} = 0 \tag{11}$$

Additionally, the ion flux and concentration must be matched at the boundaries between each domain

$$D_{e,n}\left.\frac{\partial c_e}{\partial x}\right|_{x=L_n^-} = D_{e,\text{sep}}\left.\frac{\partial c_e}{\partial x}\right|_{x=L_n^+}$$
$$c_e|_{x=L_n^-} = c_e|_{x=L_n^+}$$
$$D_{e,\text{sep}}\left.\frac{\partial c_e}{\partial x}\right|_{x=((L_{\text{sep}}+L_n)^-)} = D_{e,p}\left.\frac{\partial c_e}{\partial x}\right|_{x=((L_{\text{sep}}+L_n)^+)}$$
$$c_e|_{x=((L_{\text{sep}}+L_n)^-)} = c_e|_{x=((L_{\text{sep}}+L_n)^+)} \tag{12}$$

The potential is dependent upon the concentration according to

$$\frac{\partial \phi_e}{\partial x} = -\frac{i_e(t)}{\sigma_e} + \frac{2\overline{R}T(1 - t_0^+)}{F}(1 + \beta)\frac{\partial \ln(c_e)}{\partial x} \tag{13}$$

The activity coefficient β is treated as a tunable constant parameter, though in reality it depends nonlinearly on the lithium salt concentration. The current density in the liquid phase, i_e, is straightforward to determine by the uniform utilization assumption. The potential at $x = 0$ is set to zero since only potential differences are considered relevant when computing the cell voltage. Then Eq. (13) may be integrated directly to obtain the potential difference between $x = 0$ and $x = L_c$ after solving Eq. (10), since all terms are at minimum piecewise constant with respect to x.

4. Model order reduction

The structure of the electrochemical model described in the preceding section is summarized in Fig. 2. The three diffusion PDEs predict the transfer of ionic species in the solid phase of the two electrodes and in the liquid phase. The predicted concentrations are then used to determine the half-cell open circuit potentials and the kinetic overpotentials, through a set of nonlinear algebraic equations.

As can be observed in the block diagram, the diffusion PDEs are decoupled due to the modeling assumptions introduced in the preceding section. In fact, according to the inverted Butler–Volmer equation, Eq. (8), the kinetic overpotentials associated with charge transfer between the liquid and solid phase depend only on the concentration values at the interface, and not on the spatial distribution within the solid and liquid domains. This provides an opportunity for applying model-order reduction to obtain a computationally efficient solution. In particular, a frequency-based, realization-preserving MOR method is here applied to transform the solid and liquid diffusion PDEs into a reduced-order system of ODEs. In order to preserve the realization of the model, a Pade-series approximation is used to match the PDE-based model response in the frequency domain [16]. This approach has the advantage of retaining the physical meaning of the coefficients in the reduced-order model. Though not strictly necessary for SOC estimation, it is beneficial for applications to real-time, model-based SOH estimation.

4.1. Approximation of the solid diffusion PDE

According to Eq. (5) the lithium intercalation in the solid phase is described by a boundary value problem including a parabolic, constant coefficient PDE and two boundary conditions of the second kind. In the case of a constant current, both boundary
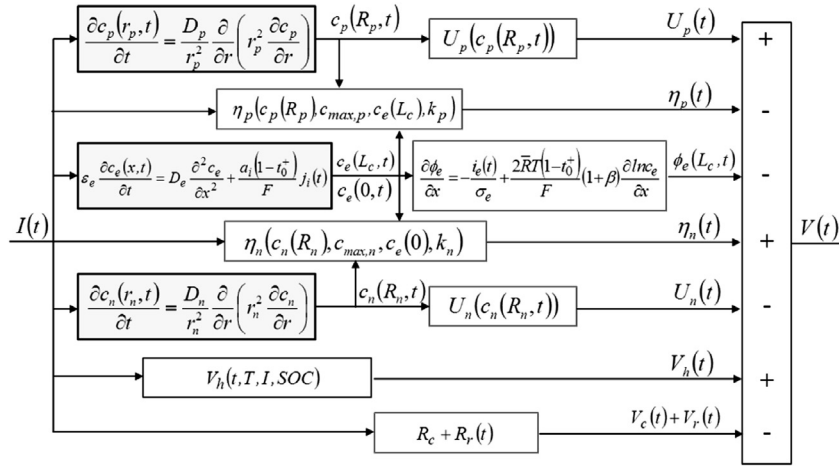
Fig. 2. Block diagram representation of the PDE-based cell electrochemical model. Scaling factors that convert the external current input to a current density are not shown for simplicity.

conditions are steady and there is an analytical solution. In general though, one boundary condition is time-varying so an analytical solution can only be obtained by applying Duhamel's superposition integral [11,43]. For estimation and control applications, a more efficient approach to obtain an approximate solution can be formulated by taking the Laplace transform of Eqs. (5) and (6) [44,45]

$$D_i \frac{d^2 C_i(s)}{dr^2} + \frac{2D_i}{r} \frac{dC_i(s)}{dr} - sC_i(s) = 0 \tag{14}$$

$$\left. \frac{\partial C_i(s)}{\partial r} \right|_{r=0} = 0, \quad D_i \left. \frac{\partial C_i(s)}{\partial r} \right|_{r=R_i} = -\frac{J_i(s)}{F} \tag{15}$$

Then introduce the transform $W_i = C_i r$ and compute the corresponding derivatives

$$\frac{dW_i}{dr} = C_i + r \frac{dC_i}{dr} \tag{16}$$

$$\frac{d^2 W_i}{dr^2} = 2 \frac{dC_i}{dr} + r \frac{d^2 C_i}{dr^2} \tag{17}$$

Dividing Eq. (17) by r and substituting into Eq. (14) gives

$$\left(\frac{d^2 W_i}{dr^2} - \frac{s}{D_i} W_i \right) = 0 \tag{18}$$

whose general solution is readily found as

$$W_i(r,s) = rC_i(r,s) = A \exp\left(r \sqrt{\frac{s}{D_i}} \right) + B \exp\left(-r \sqrt{\frac{s}{D_i}} \right) \tag{19}$$

The lithium concentration at the surface of the particle is determined by inserting the boundary conditions defined in Eq. (15) into the general solution to determine the unknown coefficients A and B, and then calculating the solution at $r = R_i$. Based on this procedure, a transcendental transfer function is obtained, relating the solid phase surface concentration to the current density

$$\frac{C_i(s)}{J_i(s)} = \frac{R_i}{D_i F} \frac{\sinh\left(\sqrt{\frac{sR_i}{D_i}} \right)}{\sqrt{\frac{s}{D_i}} R_i \cosh\left(\sqrt{\frac{s}{D_i}} R_i \right) - \sinh\left(\sqrt{\frac{s}{D_i}} R_i \right)} \tag{20}$$

Following [16,44,45], Eq. (20) is related to a diffusion-based mass transport process; hence its behavior can be modeled as a low-pass filter. This facilitates the use of a Pade approximation method to obtained a linearized representation of the model

$$\frac{C_i(s)}{J_i(s)} \approx G_i(s) = \frac{m_{0,i} + m_{1,i} + m_{2,i} + \ldots + m_{N,i}}{s(b_{0,i} + \ldots + b_{N,i})} \tag{21}$$

The coefficients of Eq. (21) can be analytically obtained from the transcendental transfer function through moment matching [16,46]. This allows the approximated model to preserve its physical consistency, through the presence of parameters such as the solid diffusion coefficient and particle radius. The coefficients for orders one to three are documented in Table 2.

The frequency responses of the transcendental PDE solution and the Pade approximate transfer functions of various orders are compared in Fig. 3.
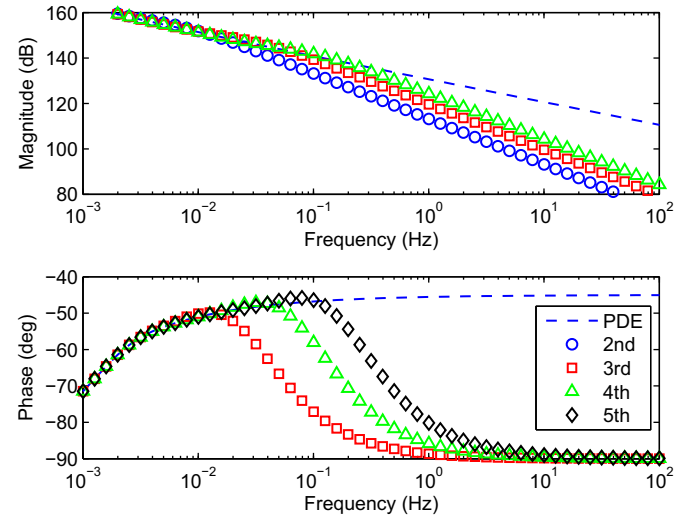
4.2. Approximation of the liquid diffusion PDE

According to Eq. (10) the lithium transport in the electrolyte is described by a parabolic PDE with homogenous boundary conditions and a spatially piecewise constant, time-varying, source term. The Laplace transform of Eq. (10) is

$$sC_e(s) - D_e \frac{d^2 C_e(s)}{dx^2} - \gamma \frac{I(s)}{AL_i a_i} = 0 \tag{22}$$

where the substitutions $\gamma = a_i(1 - t_0^+)/F\varepsilon_e$ and $j_i = I/(AL_i a_i)$ have been made to simplify notation. The boundary conditions at the cathode and anode current collectors and matching conditions at the internal boundaries (separator/anode and separator/cathode) of the cell are not repeated here because they do not change following the application of the Laplace transform. To simplify the calculation of the liquid phase transfer functions, we note that for the given cell geometry $L_n \approx 1/4L_c$, $L_{sep} \approx 3/20L_c$, $L_p \approx 3/5L_c$. Then, following the computation of the analytical solution of Eq. (22), the transfer function for the negative electrode is found by evaluating at $x = 0$

Table 2
Pade approximate transfer functions (up to third order) for the solid and liquid diffusion dynamics.

Order	Solid	Liquid, $x = L_c$	Liquid, $x = 0$
1st	$3/sR_i$	$\left(0.25\frac{L_c}{D_e}\right)\Big/\left(AF\left(1+0.112\frac{L_c^2 s}{D_e}\right)\right)$	$\left(0.33\frac{L_c}{D_e}\right)\Big/\left(AF\left(1+0.092\frac{L_c^2}{D_e}s\right)\right)$
2nd	$\left(\frac{3}{R_i}+\frac{2}{7}\frac{R_i s}{D_i}\right)\Big/\left(s\left(1+\frac{1}{35}\frac{R_i^2 s}{D_i}\right)\right)$	$\left(0.25\frac{L_c}{D_e}+0.0045\frac{L_c^3 s}{D_e^2}\right)\Big/\left(AF\left(1+0.13\frac{L_c^2}{D_e}s+0.0029\frac{L_c^4 s^2}{D_e^2}\right)\right)$	$\left(0.33\frac{L_c}{D_e}+0.012\frac{L_c^3 s}{D_e^2}\right)\Big/\left(AF\left(1+0.13\frac{L_c^2}{D_e}s+0.0029\frac{L_c^4 s^2}{D_e^2}\right)\right)$
3rd	$\left(\frac{3}{R_i}+\frac{4}{11}\frac{R_i s}{D_i}+\frac{1}{165}\frac{R_i^3 s^2}{D_i^2}\right)\Big/\left(s\left(1+\frac{3}{55}\frac{R_i^2}{D_i}s+\frac{1}{3465}\frac{R_i^4 s^2}{D_i^2}\right)\right)$	$\left(0.25\frac{L_c}{D_e}+0.0065\frac{L_c^3}{D_e^2}s+4.9\times10^{-5}\frac{L_c^5 s^2}{D_e^3}\right)\Big/\left(AF\left(1+0.14\frac{L_c^2}{D_e}s+0.0040\frac{L_c^4}{D_e^2}s^2+2.9\times10^{-5}\frac{L_c^5 s^3}{D_e^3}\right)\right)$	$\left(0.33\frac{L_c}{D_e}+0.011\frac{L_c^3}{D_e^2}s-1.5\times10^{-5}\frac{L_c^5 s^2}{D_e^3}\right)\Big/\left(AF\left(1+0.13\frac{L_c^2}{D_e}s+0.0024\frac{L_c^4}{D_e^2}s^2-2.8\times10^{-6}\frac{L_c^5 s^3}{D_e^3}\right)\right)$

Fig. 3. Frequency response of surface concentration from solid diffusion PDE and Pade approximations of various truncation order.

$$\frac{C_e(s)}{\gamma I(s)} = \frac{-12\sinh\left(\frac{7}{20}\sqrt{\frac{s}{D_e}}L_c\right)-5\sinh\left(\sqrt{\frac{s}{D_e}}L_c\right)}{3sAL_c\sinh\left(\frac{7}{5}\sqrt{\frac{s}{D_e}}L_c\right)\sinh\left(\frac{3}{5}\sqrt{\frac{s}{D_e}}L_c\right)}$$

$$+\frac{12\sinh\left(\frac{3}{5}\sqrt{\frac{s}{D_e}}L_c\right)-5\sinh\left(\frac{1}{5}\sqrt{\frac{s}{D_e}}L_c\right)}{3sAL_c\sinh\left(\frac{7}{5}\sqrt{\frac{s}{D_e}}L_c\right)\sinh\left(\frac{3}{5}\sqrt{\frac{s}{D_e}}L_c\right)}$$

$$+\frac{12\sinh\left(\frac{7}{5}\sqrt{\frac{s}{D_e}}L_c\right)-12\sinh\left(\frac{23}{20}\sqrt{\frac{s}{D_e}}L_c\right)}{3sAL_c\sinh\left(\frac{7}{5}\sqrt{\frac{s}{D_e}}L_c\right)\sinh\left(\frac{3}{5}\sqrt{\frac{s}{D_e}}L_c\right)} \quad (23)$$

Similarly, the transfer function representing the effects of the liquid diffusion dynamics on the ion concentration at the positive electrode boundary ($x = L_c$) is given by:

$$\frac{C_e(s)}{\gamma I(s)} = \frac{12\sinh\left(\frac{1}{4}\sqrt{\frac{s}{D_e}}L_c\right)+5\sinh\left(\frac{2}{5}\sqrt{\frac{s}{D_e}}L_c\right)}{3sAL_c\sinh\left(\sqrt{\frac{s}{D_e}}L_c\right)}$$

$$-\frac{5\sinh\left(\sqrt{\frac{s}{D_e}}L_c\right)}{3sAL_c\sinh\left(\sqrt{\frac{s}{D_e}}L_c\right)} \quad (24)$$

Following the same moment matching procedure discussed for the solid phase diffusion problem, a Pade approximate can be found to obtain a linear model expressing the concentration of lithium ions in the electrolyte at the current collector interface of the two electrodes, as functions of the current densities.

The frequency responses of the transcendental PDE solution and the corresponding Pade approximations are compared in Figs. 4 and 5.

The diffusion dynamics in the liquid phase exhibit behavior that is characteristic of a low-pass filter. Table 2 summarizes the transfer functions for the liquid phase for approximations up to the third order. Again, the coefficients of the transfer functions are based on the physical parameters of the unit cell model, such as the geometry, porosity, and diffusion coefficients, and any numerical
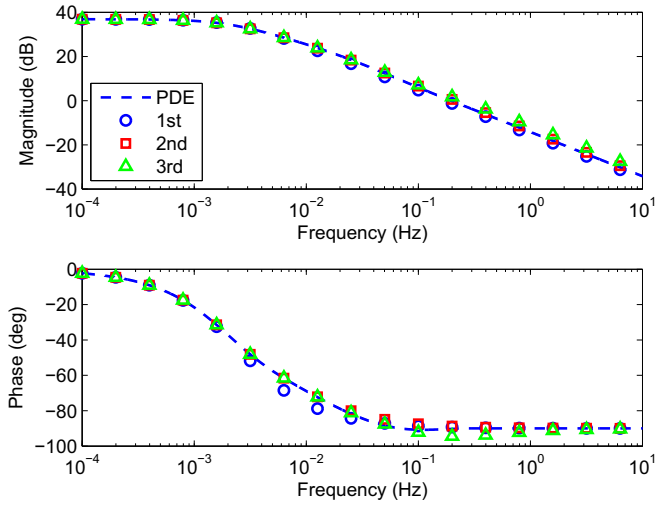
Fig. 4. Frequency response of liquid diffusion PDE for $x = 0$ and Pade approximations at various orders of truncation.

coefficients should remain constant throughout the battery's service life.

4.3. Selection of the model order

The appropriate order of each transfer function can be decided based on the frequency content of the input signal and by setting a trade-off between the number of states and the ability of the model to capture the frequency response of the PDE-based model. Based on the results shown in Figs. 3–5, the approximate transfer functions present increasing error with respect to the analytical solution as the frequency content of the input signal increases. In order to ascertain the highest desired frequency where accuracy is maintained, and therefore the approximation order, a typical current profile must be obtained from the application of interest.

To this extent, Fig. 6 shows the frequency distribution of the battery current profile obtained from a fast Fourier transform. The current profile is from experimental testing on a prototype series-parallel HEV [47] with respect to two regulatory driving cycles, namely the US06 highway cycle and the Federal Urban Dynamometer Schedule (FUDS).
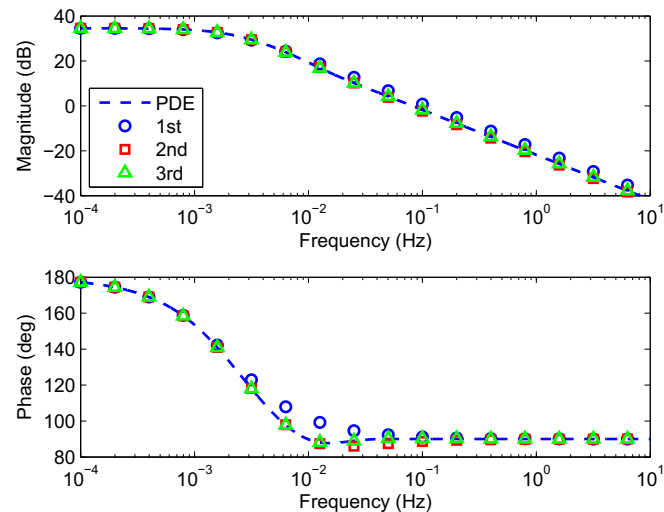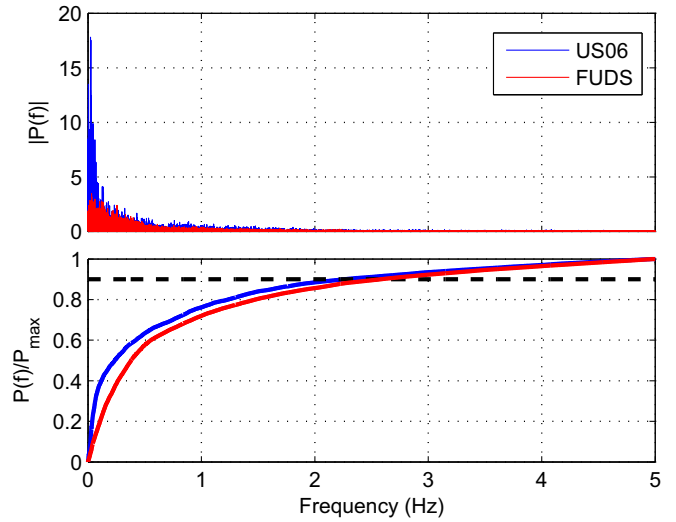

Fig. 6. Frequency content of battery current profile for charge sustaining HEV on regulatory driving cycles.

By integrating the frequency spectrum, a measure of the power contained within the signal up to a given frequency is computed. The two cases presented are quite similar, in that 90% of the signal power is within frequencies less than 2.5 Hz as indicated by the dashed line. Using this information and examining the results of the Pade approximations in Figs. 3–5, it is possible to determine an optimal order of truncation for each transfer function. Specifically, a first order truncation is chosen to model the liquid diffusion dynamics and a third order truncation is chosen for the solid diffusion dynamics.

The resulting reduced-order model is shown in Fig. 7, in block diagram form. The current input, converted to current density, feeds the reduced transfer functions calculating the boundary concentration dynamics within the solid and liquid phases. The outputs are then used to determine the concentration-dependent open-circuit potentials and charge transfer overpotentials, through nonlinear algebraic functions. Note that the procedure above described can be easily extended to other current profiles for electrified vehicles, based on regulatory cycles or fleet data, and
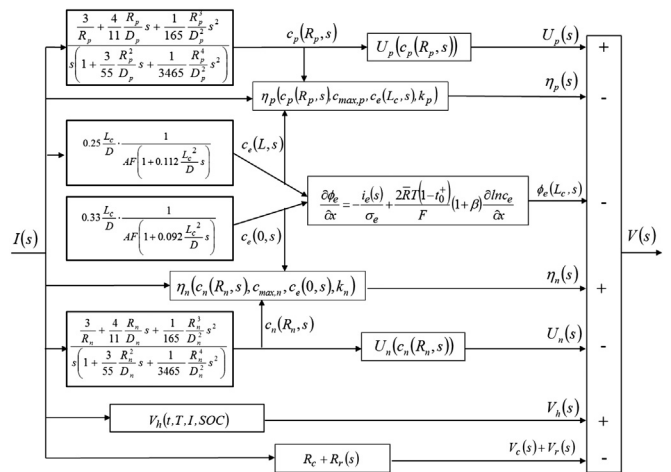

Fig. 5. Frequency response of liquid diffusion PDE for $x = L_c$ and Pade approximations at various orders of truncation.

Fig. 7. Block diagram representation of the reduced cell electrochemical model. Scaling factors that convert the external current input to a current density are not shown for simplicity.

that the two federal cycles considered here are only exemplary cases.

5. Model parametrization analysis

This section illustrates the procedure for defining the model parameters, based on non-linear identification techniques. Rather than fitting all parameters purely through optimization methods, an attempt is here made to carefully exercise the system with selected experimental inputs so as to limit the number of parameters that influence the output voltage, then identify that subset of parameters from experimental data. This approach has the advantage of providing a trade-off between two prevalent approaches, namely pure nonlinear identification from cell-level performance data and extensive experimental characterization using half-cell testing. Though more intuition regarding the electrochemical dynamics of the system is required as compared to a numerical approach, the procedure still relies mostly on cell-level performance data with the exception of utilizing half-cell OCV curves.

First the active volume fractions and composition ranges of the positive and negative electrodes are estimated from cell OCV data. During this process, the maximum hysteresis voltage is characterized as a function of temperature and SOC. Next, resistance parameters are estimated from galvanostatic cycling data over a wide range of temperatures. Lastly, the diffusion parameters are identified through a combination of literature sources and tuning to match experimental voltage relaxation data. The capacity utilization from multi-rate capacity tests are combined with an inverse model to compute the negative electrode diffusion coefficient, and current pulses are used to modify the liquid phase diffusion and activity coefficients after selecting values from literature as a useful starting point.

5.1. Identification of capacity-related parameters

The OCV for the cell model can be found starting from the OCV curves relative to Li/Li$^+$ for the positive and negative electrodes, obtained experimentally from half-cell testing or from literature. In detail, the functional form of the positive OCV [39] is

$$U_p(y) = 3.432 - 0.843e^{-80.249(1-y)^{1.319}} - 3.247$$
$$\times 10^{-6}e^{20.264(1-y)^{3.800}} + 3.2482 \times 10^{-6}e^{20.264(1-y)^{3.799}}$$

(25)

Similarly, the functional form of the negative OCV [39] is

$$U_n(z) = 0.638 + 0.542e^{-305.5309z} + 0.044\tanh\left(-\frac{z-0.196}{0.109}\right)$$
$$- 0.198\tanh\left(\frac{z-1.057}{0.085}\right) - 0.686\tanh\left(\frac{z+0.012}{0.053}\right)$$
$$- 0.018\tanh\left(\frac{z-0.569}{0.086}\right)$$

(26)

Fig. 8 shows the OCV curves for the positive and negative electrode.

While the OCV of each electrode is known, the composition range determined by the initial degree of lithiation and the active volume fraction of each electrode must still be identified using full-cell OCV data. To this extent, an experimental procedure was conducted where the cell is first discharged to the lower voltage limit of 2.0 V. Then a charge current pulse is executed to add 5−10% capacity to the cell, followed by a wait period of 1 h to allow the
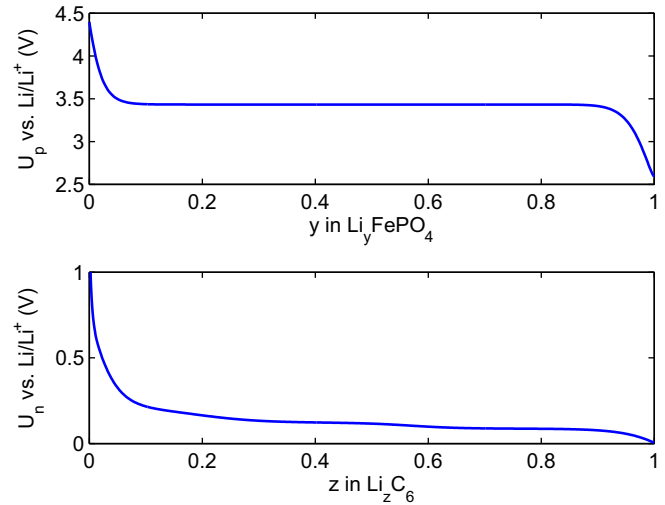

Fig. 8. Open-circuit voltage curves for positive and negative electrode.

cell to reach equilibrium. The cell voltage after 1 h is recorded as the OCV for the appropriate SOC based on current integration. This procedure is repeated until the upper voltage limit of 3.6 V is reached. Then, the current direction is reversed and the entire process is repeated to assess the amount of hysteresis associated with the cell OCV. The described procedure allows the identification of the model parameters related to the scaling and initial conditions of the half cell potentials while eliminating the influence of the any overpotential on the output voltage.

The mean of the charge and discharge OCV data is the input to a nonlinear least square procedure to perform the estimation of the electrode composition ranges. The algorithm consists of finding the optimal set of parameters $\overrightarrow{P}^* = [z_0^*, y_0^*, \varepsilon_n^*, \varepsilon_p^*]$ minimizing the cost function in Eq. (27), where the error $\overrightarrow{e}$ is a vector of differences between the experimental OCV data and the predicted OCV ($\overrightarrow{e}(\text{SOC}) = V_{\exp}(\text{SOC}) - V(\text{SOC})$). The nonlinear least square problem is cast as follows:

$$\overrightarrow{P}^* = \underset{[z_0^*, y_0^*, \varepsilon_n^*, \varepsilon_p^*]}{\operatorname{argmin}} \left(\frac{1}{2}(\Delta\overrightarrow{P})^T \frac{\partial^2 \overrightarrow{e}}{\partial \overrightarrow{P}^2}(\Delta\overrightarrow{P}) + (\Delta\overrightarrow{P})^T \frac{\partial \overrightarrow{e}}{\partial \overrightarrow{P}}\right)$$

(27)

The experimental OCV data and the fitted model OCV resulting from the solution of Eq. (27) are plotted in Fig. 9. The maximum hysteresis voltage is calculated as one half the difference between the charge and discharge OCV data at each SOC. After observing the trend of the experimental data, it is fit with a linear function,

$$H(T, \text{SOC}) = h_1(T) \times \text{SOC} + h_2(T)$$

(28)

where h_1 and h_2 are identified for various temperatures to create a one-dimensional interpolation table. The resulting linear fit for the 20 °C case is also plotted in Fig. 9. There are cyclic variations from the overall linear trend that are believed to arise from experimental error associated with the current integration procedure, preventing the selection of exactly the same SOC set point when approaching from charge and discharge directions. Since these are believed to be associated with experimental error and not an actual electrochemical feature, the linear fit of maximum hysteresis voltage is considered sufficient. Other temperatures showed qualitatively similar agreement with the linear function, as the hysteresis calculation is repeated for 5 °C, and 55 °C data, and a linear fit of maximum hysteresis with respect to SOC is calculated
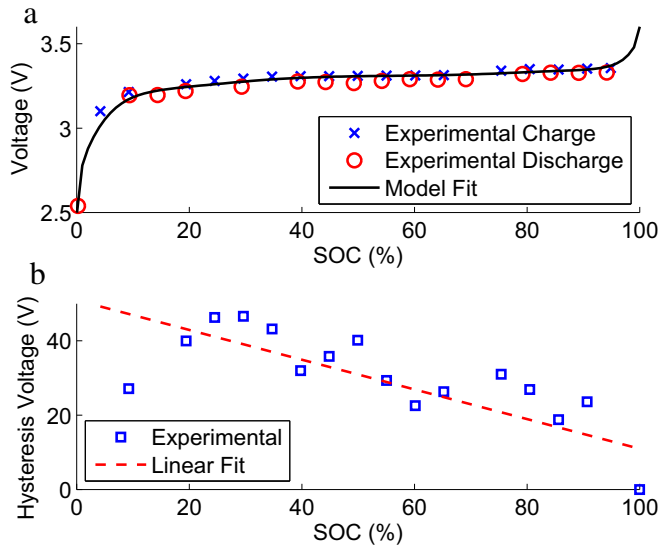
Fig. 9. a) Experimental OCV data and model fitted to mean of charge and discharge data, where measurements taken while traversing the SOC range from 0% toward 100% are indicated as 'Experimental Charge', and those from 100% toward 0% are denoted 'Experimental Discharge'. b) Hysteresis voltage and linear fit with respect to SOC.

for each temperature. The fitting parameters are summarized in Table 3.

It is assumed that the half-cell OCV and composition ranges do not vary over the temperature range from 5 °C to 55 °C. Verification of this assumption is possible using extensive half-cell fabrication and testing at multiple temperatures. However, this is considered outside the scope of this paper and model agreement is acceptable without modifying the OCV or estimated composition range to consider temperature dependence within the presented range.

5.2. Identification of resistance-related parameters

The objective of this section is to identify the temperature dependence of the parameters responsible for determining the time-varying cell resistance, including the ohmic resistance, the kinetic rate constants of each electrode, the activity coefficient of the liquid, and the diffusion coefficients in each phase.

5.2.1. Initial overpotential

As a current input is introduced, both ohmic and kinetic resistances contribute in determining the cell terminal voltage. In general it is difficult to determine each electrode rate constant and the remaining ohmic resistance without half-cell testing or literature data. Here, a novel method is proposed that takes advantage of the nonlinearity associated with the kinetic overpotential [48] to distinguish between ohmic and kinetic resistance. This nonlinearity, when combined with careful assumptions and experimental data for a range of temperature conditions, allows for the individual identification of the Arrhenius dependence of the rate constants for each electrode and the remaining ohmic component of resistance.

Table 3
Summary of hysteresis parameters as a function of temperature.

Temperature	h_1	h_2
5 °C	-2.4×10^{-4}	6.02×10^{-2}
20 °C	-4.0×10^{-4}	5.09×10^{-2}
55 °C	-3.0×10^{-4}	3.95×10^{-2}

For this procedure, it is assumed that the kinetic overpotential of each electrode is negligible above a certain reference temperature. This assumption takes advantage of the strong variation of the exchange current with respect to temperature that most Li-ion chemistries exhibit. Experimentally, a variation of resistance with respect to current is observed at low temperature conditions, which is assumed to be directly related to the exchange current density via the kinetic rate constant.

For the negative electrode, a reference temperature of 20 °C is assumed, since typically the negative electrode does not contribute significantly to the cell overpotential at room temperature [49]. For the positive electrode the reference temperature is selected as 55 °C, and though this choice is arbitrary it reflects two key considerations. First, the kinetic overpotential of the positive electrode is non-negligible at room temperature. Second, there should be a limiting temperature where kinetic overpotential from the positive electrode is no longer a factor. An Arrhenius temperature dependence is assumed of the form

$$P = P_1 \exp\left(-\left(\frac{P_2}{T} - \frac{P_2}{T_{\text{ref}}} \right)^{P_3} \right) \tag{29}$$

where P_1 fixes the parameter value at the reference temperature, P_2 is the activation energy that governs the temperature dependence of each parameter, and P_3 is a unitless number that is useful in obtaining agreement with experimental data in non-ideal cases. Since there has been supporting data in literature [50] for a unity value of P_3 as applied to the temperature dependence of kinetic rate constants, we fix $P_3 = 1$ for both the positive and negative rate constants. However, commonly used positive electrode active materials have displayed similar electronic conductivity properties to semiconductors [51]. A non-unity P_3 is useful in situations where there may be a range of activation energies for a given process, such as those associated with semiconductor-like behavior such as ion-hopping [52]. The ohmic fit accounts at least partially for the active material conductivity, so the ohmic fitting procedure allows for $P_3 \neq 1$. The functional form of Eq. (29) is also used to describe the temperature dependence of the diffusion and activity coefficients discussed in later sections.

The conducted experiments gathered resistance data for temperatures of −10, 5, 20, 35, and 55 °C. For each temperature, currents from 1C to 10C are tested, except at −10 °C, where current is limited to 5C due to power limitations at cold temperatures. To begin, the positive electrode characteristics are isolated by using data from each temperature above 20 °C. The variation in resistance with respect to current is computed using Eq. (30)

$$\Delta(R) = R|_{10C} - R|_{1C} = \left(\frac{1}{I|_{10C}} \frac{\bar{R}T}{F} \sinh^{-1}\left(\frac{j_p|_{10C}}{2i_{0,p}} \right) \right) - \left(\frac{1}{I|_{1C}} \frac{\bar{R}T}{F} \sinh^{-1}\left(\frac{j_p|_{1C}}{2i_{0,p}} \right) \right) \tag{30}$$

Note that the contact resistance and ohmic contributions from the liquid phase are not included. This is because they do not change with respect to current, and so they do not impact Eq. (30). All parameters in Eq. (30) are fixed except for the exchange current density, or equivalently the rate constant. Various values of the rate constant may be selected to effectively vary the exchange current density and produce different values of $\Delta(R)$. After matching the experimental $\Delta(R)$ for temperatures above 20 °C, where the negative electrode kinetic overpotential is neglected, a positive electrode rate constant associated with each tested temperature is

found. The resulting data are fit using Eq. (29) to provide a smooth interpolation and extrapolation function.

For temperatures below 20 °C, the positive temperature dependence identified for temperatures above 20 °C is extrapolated and included in the total overpotential. Then the variation of resistance with respect to current is fit using the negative rate constant, using a similar procedure to the positive electrode with Eq. (31) replacing Eq. (30).

$$
\begin{aligned}
\Delta(R) &= R|_{10C} - R|_{1C} \\
&= \frac{1}{I|_{10C}} \left(\frac{\overline{R}T}{F} \sinh^{-1}\left(\frac{j_p|_{10C}}{2i_{0,p}} \right) + \frac{\overline{R}T}{F} \sinh^{-1}\left(\frac{j_n|_{10C}}{2i_{0,n}} \right) \right) \\
&\quad - \frac{1}{I|_{1C}} \left(\frac{\overline{R}T}{F} \sinh^{-1}\left(\frac{j_p|_{1C}}{2i_{0,p}} \right) + \frac{\overline{R}T}{F} \sinh^{-1}\left(\frac{j_n|_{1C}}{2i_{0,n}} \right) \right)
\end{aligned} \tag{31}
$$

The curves of resistance variation versus rate constant value for each electrode are plotted in Fig. 10.

Due to the superior surface area per unit volume of the iron phosphate positive electrode, the rate constant values are generally smaller than those of the negative electrode to achieve a similar level of resistance variation. Once the rate constant identification procedure has been completed, the kinetic component of the cell resistance is known. The temperature dependence of the ohmic resistance must account for the remaining portion of the resistance data. Here, a nonlinear least-squares problem is formulated as

$$
\begin{aligned}
\overrightarrow{P}^* &= \operatorname*{argmin}_{[R_{c,1}, R_{c,2}, R_{c,3}]} \left(R_{exp}(I,T) - R_{c,1} \exp\left(-\left(\frac{R_{c,2}}{T_{ref,R_c}} - \frac{R_{c,2}}{T} \right)^{R_{c,3}} \right) \right. \\
&\quad - \frac{1}{I}\frac{\overline{R}T}{F}\sinh^{-1}\left(\frac{I}{2i_{0,p}} \right) - \frac{1}{I}\frac{\overline{R}T}{F}\sinh^{-1}\left(\frac{I}{2i_{0,n}} \right) \\
&\quad \left. - \left(\phi_e\left(L_c, 0^+ \right) - \phi_e\left(0, 0^+ \right) \right) \right)
\end{aligned} \tag{32}
$$

The liquid phase ohmic contributions, represented by $(\phi_e(L_c, 0^+) - \phi_e(0, 0^+)(T))$, are computed from the ohmic term of Eq. (13) with the notation of $t = 0^+$ indicating the result is taken immediately following the onset of current. Concentration

Fig. 11. Comparison of experimental resistance data with fitted model prediction.

overpotential is irrelevant since the instantaneous resistance is being considered. The conductivity properties as a function of temperature are taken directly from Ref. [53]. The rest of the parameters have been identified by the preceding analyses leaving $R_{c,1}$, $R_{c,2}$, and $R_{c,3}$ for identification. Fig. 11 shows the final comparison between experimental resistance recorded for each temperature and the model fit. The identification procedure reveals that the stretched exponential coefficient is non-zero for the contact resistance. This is required to achieve agreement with the data after identifying the Arrhenius dependence of the rate constants and has occasionally been observed for the electronic conductivity of Li-based systems [54]. The variation of resistance with respect to current is captured well even for the most severe case at −10 °C, where the total variation is over 20 mΩ. Table 4 summarizes the Arrhenius coefficients for each parameter that exhibits temperature dependence.

5.2.2. Time-varying ohmic overpotential

As discussed during the model development, there are increasing ohmic contributions during a charge or discharge current pulse related to the poor electronic conductivity of iron phosphate. The conductivity of the positive electrode is identified empirically, since it is composed of several constituents of vastly different properties making it difficult to predict without experimental data. To perform the fitting procedure, the identified capacity and initial resistance parameters are used to model a low-rate (≤1C) galvanostatic discharge. The iron phosphate conductivity is considered constant with respect to SOC, since it has been reported previously that it does not change with composition [55]. The region for parameter identification is restricted to 0.2–1.6 Ah. This is because the middle portion of the discharge curve is less prone to transient errors from the effects of slightly imperfect
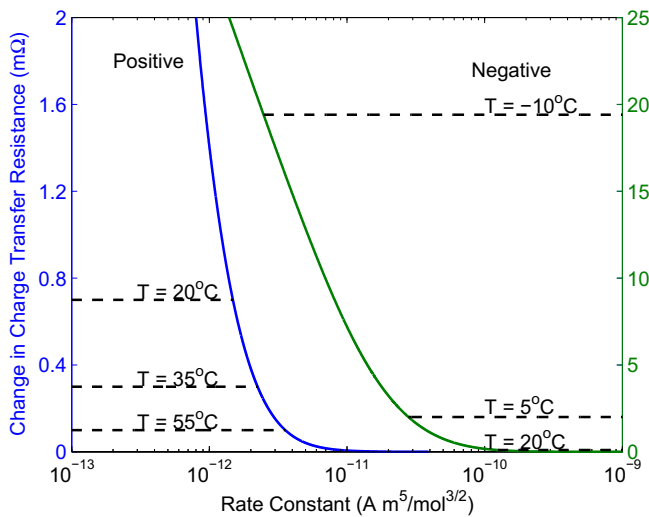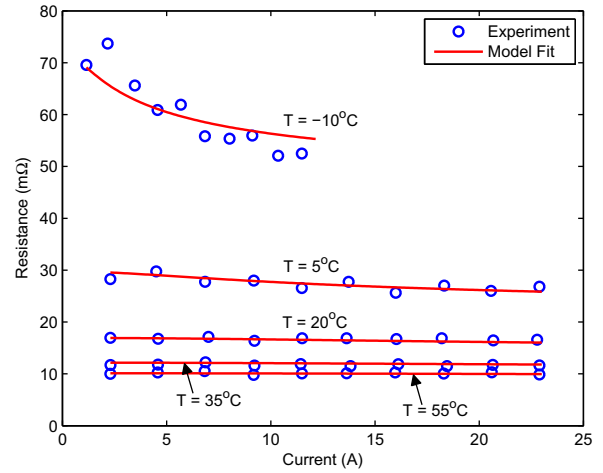

Fig. 10. Variation of the resistance between 1C and 10C current pulses versus the required rate constant to achieve the resistance variation. Dashed lines indicate the experimentally observed level of variation at each temperature and intersect the electrode to which the variation is attributed.

Table 4
Arrhenius coefficients of parameters that vary with respect to cell temperature.

Parameter	R_1	R_2	R_3	T_{ref}
R_c	8.24×10^{-3}	1740	1.96	328
σ_p	7.6×10^{-7}	1740	1.96	328
k_n	1.8×10^{-6}	7120	1.00	268
k_p	2.9×10^{-7}	1860	1.00	328
D_n	1.9×10^{-14}	2050	1.00	293
D_e	3.6×10^{-11}	10,000	0.50	262
β	2.35	140	0.30	338

initial conditions that may cause large errors in predicted voltage at the beginning and end of the discharge process. The error between the model prediction and experimental data tends to increase linearly for a fixed current value as charge is removed from the cell. It may be fit by solving the linear least squares problem

$$V_r(t) = V_{r,0} + \frac{L_{\text{cond}}(t)}{a_p L_p A} \frac{I}{\sigma_p} \tag{33}$$

Here V_r is the overpotential error and $V_{r,0}$ is the initial unmodeled overpotential (the value at $Q = 0.2$ Ah). When solving the least squares problem, $V_r(t)$ is a vector of values corresponding to the difference between the experimental data and model predicted voltage. The constant term $V_{r,0}$ is subtracted from the vector $V_r(t)$ to form a vector $\tilde{V}_r(t)$, and t is a vector of time values corresponding to $\tilde{V}_r(t)$. The solution to the least squares problem is given by

$$\sigma_p = \left(\tilde{V}_r(t)(M)^T \left(M(M)^T \right)^{-1} \right)^{-1} \tag{34}$$

where $M = \frac{1}{I} \frac{a_p L_p A}{L_{\text{cond}}(t)}$. Inserting values for the known constants gives $\sigma_p = 7.6 \times 10^{-7}$ S m^{-1}, which is within the range of values reported in literature [56] given that the exact amount of conductive carbon additive is unknown. Fig. 12 shows the error as a function of discharge capacity and the model fit to the error used to select a conductivity value. Although the identification procedure is performed only for 20 °C, it is assumed that this conductivity value shares the same temperature dependence as the initial ohmic resistance, since theoretically these phenomena are related.

5.3. Diffusion parameters

The solid diffusion coefficient of the negative electrode is tuned to match the experimentally observed difference in capacity between the C/3 and 1C rates, after fixing the particle size to a typical literature value. This may be approached quantitatively through the use of an inverse function, where the analytical solution of Eq. (5) for a constant current is related to the potential of the negative electrode at the end of discharge to ascertain the end-of-discharge Li$^+$ concentration, and therefore the diffusion coefficient. The analytical solution for the non-homogeneous, steady boundary condition case of Eq. (5), where $F_0 = -\partial c_n/\partial r|_{r=R_n}$, is

$$(c_n(r,t) - c_n(r,0)) \frac{D_n}{F_0 R_n} = \frac{3 D_n t}{R_n^2} + \frac{1}{2} \frac{r^2}{R_n^2} - \frac{3}{10}$$
$$- 2 \frac{R_n}{r} \sum_{j=1}^{N} \left(\frac{\sin(\lambda_j r)}{\lambda_j^2 R_n^2 \sin(\lambda_j R_n)} \exp\left(-D_n \lambda_j^2 t\right) \right) \tag{35}$$

The λ_j coefficients are given by the positive roots of

$$R_n \lambda_j \cot(R_n \lambda_j) = 1 \tag{36}$$

where an arbitrary number of terms of the infinite eigenvalue series may be used. Analysis of the required number of eigenvalues indicated that there are minimal accuracy gains beyond 10 terms. The goal is to use Eq. (35) to identify the diffusion coefficient by relating the concentration at the end of discharge and the current magnitude to the diffusion coefficient. The input to the procedure is the external current for the capacity test, which fixes F_0 to a constant value. Based on experimental measurement, the total time of the capacity test t_f is known. The voltage at the end of the capacity test is dictated by the lower voltage limit. Rearranging the terminal voltage expression in terms of the limiting concentration at the end of discharge, $c_n(R_n, t_f)$, gives

$$c_n\left(R_n, t_f\right) = c_{\max,n} U_n^{-1} \left(U_p\left(t_f\right) - \left(\phi_e\left(L_c, t_f\right) - \phi_e\left(0, t_f\right)\right) \right.$$
$$- \left(\eta_p\left(t_f\right) - \eta_n\left(t_f\right)\right) - \left(R_r\left(t_f\right) + R_c\right) I - V_h\left(t_f\right)$$
$$\left. - V_{\min} \right) \tag{37}$$

This procedure assumes that the negative electrode OCV is invertible, which is typically a good assumption at the end of discharge away from the characteristic plateaus found for higher composition values. The limiting concentration values for each current are plotted as horizontal lines in Fig. 13. The limiting concentration as a function of the diffusion coefficient is also plotted by sweeping Eq. (35) over a range of values for D_n. The intersection of the symbols with the limiting concentration lines gives the diffusion coefficient that precisely matches the experimentally observed capacity for each rate. If the model perfectly reflected the electrochemistry occuring within the cell, the value of the diffusion coefficient predicted by this method would be constant regardless of rate. Regardless the predicted values are close and an average
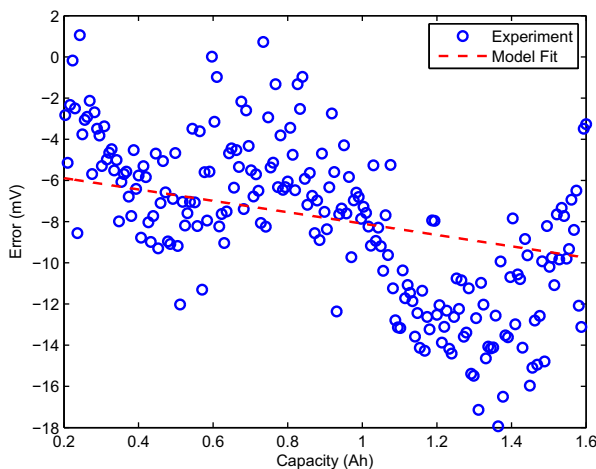

Fig. 12. Error as a function of capacity removed during a galvanostatic discharge and model prediction of resistive reactant overpotential after identification of positive electrode conductivity.
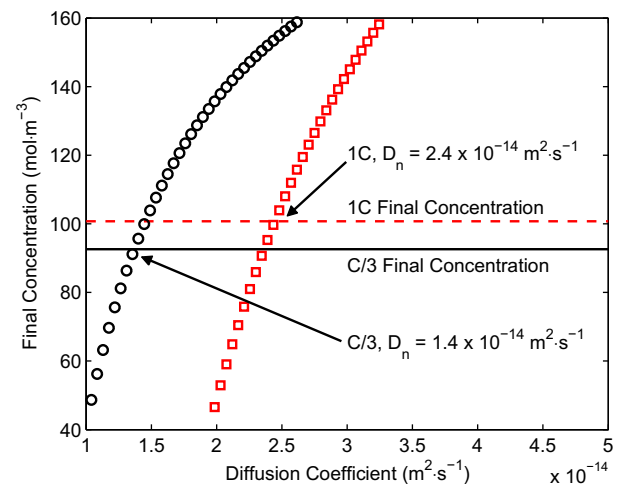

Fig. 13. Negative electrode diffusion coefficient identification via inversion of the spherical diffusion analytical solution for a steady boundary flux. Lines indicate the final concentration for each current, defined by Eq. (37), and the symbols indicate the final concentration predicted by Eq. (35) as a function of the diffusion coefficient.

may be used without introducing significant model error. The agreement obtained by the diffusion coefficient tuning procedure is shown in Fig. 14.

Once the diffusion coefficient has been identified for room temperature, the temperature dependence is estimated based upon comparisons with capacity tests conducted at the same rate, but varying temperatures. The resulting Arrhenius coefficients are documented in Table 4. The positive diffusion coefficient is set to a literature value since the complex phase change process of iron phosphate is not modeled. This omission, when combined with the characteristic plateau of the iron phosphate OCV, renders the model voltage prediction somewhat insensitive to the value of the positive diffusion coefficient. However it is noted that the selected diffusion coefficient gives qualitative agreement with the behavior at various current rates in the solid solution region at high cell SOC (low positive electrode composition) near 20 °C.

The diffusion coefficient, transference number, and activity coefficient of $LiPF_6$-based electrolyte have been experimentally characterized as a function of concentration and temperature for standard carbonate solvents [53]. To incorporate their results into the simplified modeling approach of this work, the parameter values from the equivalent nominal concentration value of 1 mol L^{-1} are used.

The reported diffusion coefficient is combined with an assumed Bruggeman coefficient of 2.8 [57] and an experimentally tuned porosity value to compute the effective diffusion coefficient. Given the unhindered value of 1.5×10^{-10} m^2 s^{-1} reported in Ref. [53], a porosity value of 0.52 gave good agreement with the time constant of relaxation following interruption of current. While the time constant is governed by the effective diffusion coefficient, the magnitude of the relaxation voltage is determined by the activity coefficient. It was found that a higher activity coefficient than reported in Ref. [53] resulted in better agreement with the experimental data through greater diffusion overpotential in the liquid phase. This could be possible for several reasons. First, the activity coefficient of the present model does not vary with concentration, and the local concentrations at either end of the cell during high current operation could be much different than the nominal value, which in turn would lead to greater potential variation if a concentration-dependent activity coefficient were used. Another possible reason for the increased activity coefficient could be that some dynamics associated with the OCV hysteresis are being assigned to

the liquid phase. For instance, other authors have characterized a hysteresis effect with a time constant much smaller than the long-term effect modeled in this work [40], and the larger activity coefficient could be partly accounting for the fast initial relaxation of the OCV hysteresis. Note that the solid diffusion coefficients had been previously identified and their effects are inherently included when obtaining agreement between model and experiment during voltage relaxation. Additional model parameters that are taken as independent of temperature are summarized in Table 5.

6. Results, and discussion

This section compares the model performance with experimental data to validate the preceding methodology. A variety of charge sustaining (CS) and charge depleting (CD) experiments are performed. The two quantitative error metrics are the root-mean-square (RMS) error and 95th percentile error, indicating 95% of observed error is less than the reported value.

6.1. CS operation

The first set of validation data, meant to imitate CS HEV operation, is comprised of constant current pulses of magnitudes ranging from 1C to 10C. The time duration of each pulse is set to achieve a change in SOC of 10%. Each discharge pulse is followed by a corresponding charge pulse such that the overall profile is charge neutral about a given SOC. After several charge neutral pulses about a given SOC, a 1C current is used to set SOC for the next set of current demands followed by a 30 min rest period to ensure the system reaches equilibrium. There is a constant voltage portion near 480 min as the cell reaches its upper voltage limit. Model agreement is not demonstrated in this region, as the current relaxation predicted by the model is much faster than suggested by the experimental data. A HEV would operate in a region from approximately 80% SOC to 20% SOC and should not expect to see constant voltage charging, so the model is still considered useful despite this shortcoming. The overall current profile and the corresponding SOC trajectory are plotted in Fig. 15.

These inputs are applied for temperatures of 5 °C, 20 °C, and 55 °C. Fig. 16a–c compare the model prediction with experimental data for these three cases respectively, for a SOC of 40%. The model accuracy for other SOC conditions is documented in Table 6.

Examining the voltage response in detail, it becomes apparent that the initial overpotential upon application of a current demand is predicted well for all temperatures considered. This validates the resistance parameter identification procedure from a system performance prediction standpoint, though admittedly it cannot be determined whether the extracted Arrhenius coefficients correspond to the true nature of each parameter or simply provide agreement with the experimental data. The inclusion of the liquid phase concentration and potential dynamics leads to significantly more accurate prediction of the cell voltage during the relaxation phase following current interruption and for high current conditions.
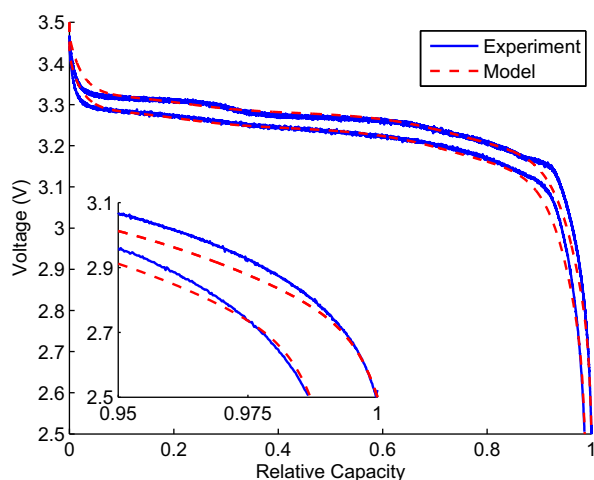

Fig. 14. Relative capacity utilization for two examples of low rate galvanostatic discharge. The identified negative diffusion coefficient, $D_n = 1.9 \times 10^{-14}$ m^2 s^{-1}, matches the capacity decrease when comparing C/3 to the 1C rate.

Table 5
Summary of model parameters taken as independent of operating conditions.

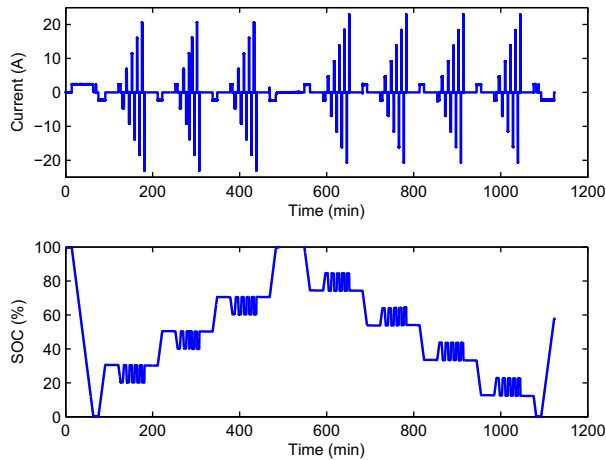| Parameter	Definition	Value
ε_n	Negative active volume fraction	0.35
ε_p	Positive active volume fraction	0.35
z_0	Initial negative composition	0.74
y_0	Initial positive composition	0.026
t_0^+	Transference number of Li^+	0.39
α	Butler–Volmer transfer coefficient	0.5
ε_e	Liquid volume fraction	0.52
brug	Bruggeman coefficient	2.8

Fig. 15. Input current profile and SOC trajectory for CS validation.

Based on the results shown, it is evident that the model provides better agreement at 20 °C than at the two extreme temperatures, though the results are better for 55 °C than for 5 °C. The reason for this may be the discrepancies between the fitted OCV, recorded at 20 °C, and the experimental values begin to become more significant for extreme temperatures. The noted discrepancies could be related to changes in the thermodynamic OCV driven by entropy considerations or simply a more pronounced hysteresis phenomena. There is also a general tendency to overpredict the overpotential during charging for low-temperature operation. As a result, though the initial resistance is accurately captured at temperatures down to −10 °C using the documented identification procedure, these limitations create a practical lower temperature bound around 5 °C for validating the model predictions. This does not pose a serious practical concern, since most systems will be severely power limited below 5 °C and it may be expected that a satisfactory thermal management system will prevent the battery temperature from reaching such low levels.

Following authors who have examined the sources of overpotential using porous electrode models [41,49], we illustrate the relative magnitude of each overpotential source during a 10C discharge beginning from 50% SOC, at 20 °C, in Fig. 17. The discharge duration is chosen to remove 10% SOC from the cell, similar to the current demands of the CS validation profile.

The dominant source of overpotential is the contact resistance, which also includes the lumped effect of the initial ohmic resistance of the solid matrix in this model structure. The time-varying solid phase ohmic losses, referred to interchangeably as the resistive reactant effect, contribute a minor amount of overpotential in this case because of the short duration of the current pulse. During longer current pulses, such as the limiting case of a constant current capacity test discussed previously, the resistive reactant overpotential becomes more apparent. As expected, positive kinetic losses are greater than those in the negative electrode, though neither is as large as the ohmic losses since the example is taken at 20 °C. Liquid ohmic losses are of the same order as the kinetic losses, and liquid phase diffusion contributes a fair amount to the total overpotential since the current rate is high. The overpotential from the liquid also tends to increase continually indicating that a steady profile is not reached by the end of the pulse duration. Finally, the solid diffusion overpotential of either electrode is surprisingly small, despite the formation of significant concentration gradients as is expected for high current rates. The lack of overpotential is due to the minimal variation of each half-cell OCV with respect to composition, and should not be interpreted as the solid
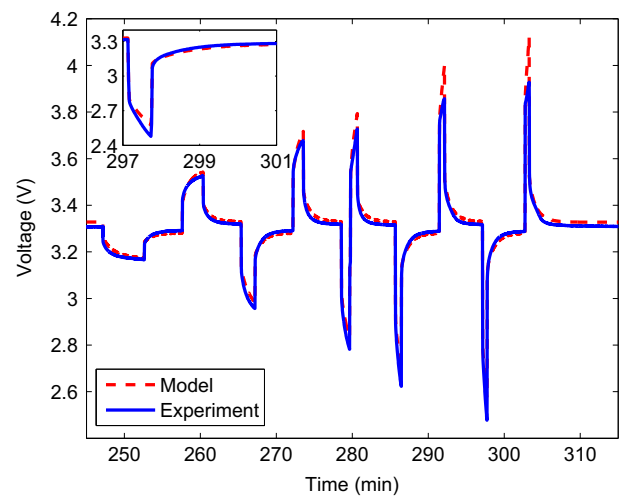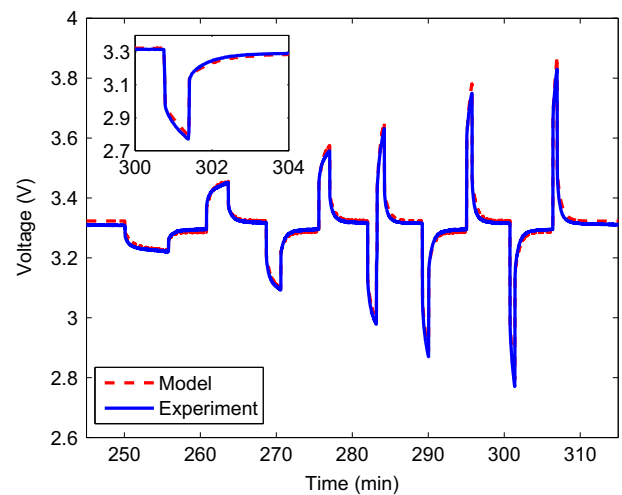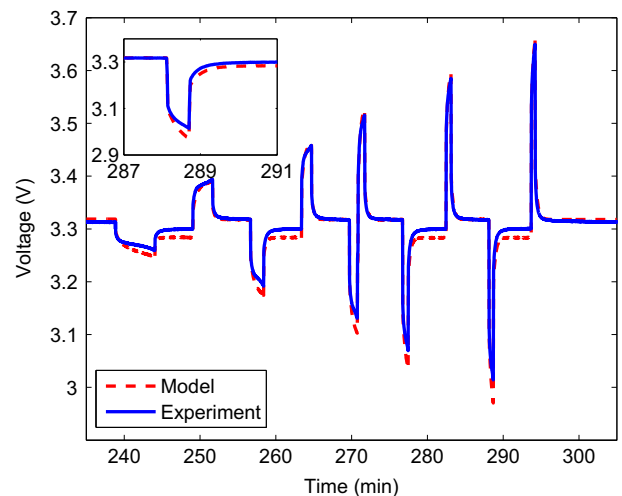
Fig. 16. Comparison of model predictions with experimental data for charge sustaining profile and temperatures of a) 5 °C, b) 20 °C, c) 55 °C.

Table 6
Summary of model error for CS operation, reported as RMS/95th percentile (mV).

Temperature (°C)/SOC (%)	15	20	35	40	55	60	75
5	24.7/55.2	27.8/49.3	30.9/61.7	27.6/46.6	37.1/69.7	29.8/57.4	27.3/55.0
20	21.7/42.1	17.0/36.3	14.9/31.7	13.9/29.0	19.3/39.8	14.8/34.8	9.8/21.0
55	15.7/26.0	9.2/21.4	9.5/20.2	13.0/23.7	8.1/17.0	7.7/17.8	9.7/20.5

phase having faster diffusion than in the liquid. There are significant concentration gradients present in the solid, but the opportunities for developing overpotential are less.

Upon interruption of the current, the ohmic and kinetic contributions vanish. The subsequent relaxation phase is dominated by the decay of the liquid phase concentration gradients. The solid concentration overpotential relaxes more quickly, again due to the minimal variation of each half-cell OCV with respect to composition and not because the solid concentration gradient relaxes more quickly than in the liquid. The hysteresis effect is also visible, causing a lower voltage than predicted by the bulk SOC change of the electrode even after complete relaxation of the solid and liquid phase concentration gradients.

6.2. CD operation

Validation results are also included for a CD profile to ensure that the model maintains sufficient performance predictions for current profiles that are not centered about a single SOC point. The profile is extracted from the United States Department of Energy battery test manual for PHEVs [36]. The current and SOC trajectories are plotted in Fig. 18. Similarly to the CS validation, these experiments are repeated at temperatures of 5 °C, 20 °C, and 55 °C.

Fig. 19 shows the model voltage prediction and experimental data for the CD profile at 55 °C.

The model performance is acceptable, though it is worth discussing two instances where the errors between model and experimental data are largest. In the initial portion of the profile, there are some brief transient errors at high SOC. These could be related to the neglect of the temperature dependence of the Li^+ diffusion coefficient for Li_yFePO_4. The second instance of notable model error is during the latter stages of the profile, where cell SOC is low. Throughout most of the profile, it appears there is a steady offset between the model prediction and experimental data, though transient overpotential is still captured well. The steady nature of the error indicates inaccurate SOC prediction in either of

the two electrodes leading to inaccurate OCV, insufficient characterization of the dependence of the OCV on temperature, or insufficient hysteresis modeling.

The first two hypotheses can be eliminated in light of the charge sustaining operation data. If they did contribute to the model error at low SOC, it would have been revealed by the data plotted in Fig. 16 and documented in Table 6; however, model performance is better there than exhibited during CD operation. The characterization of the hysteresis used relatively short duration current pulses that caused no greater than a 10% change in SOC. The CD profile, although not a continuous discharge, is overall charge depleting for a duration of 1 h and therefore may be incurring some greater amount of hysteresis than captured by previous experiments.

Similarly to the CS profile, the overall cell resistance is over-predicted during the high current demands of the profile, more so
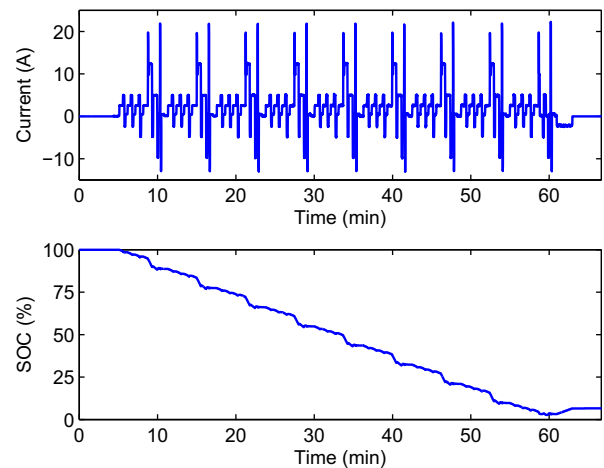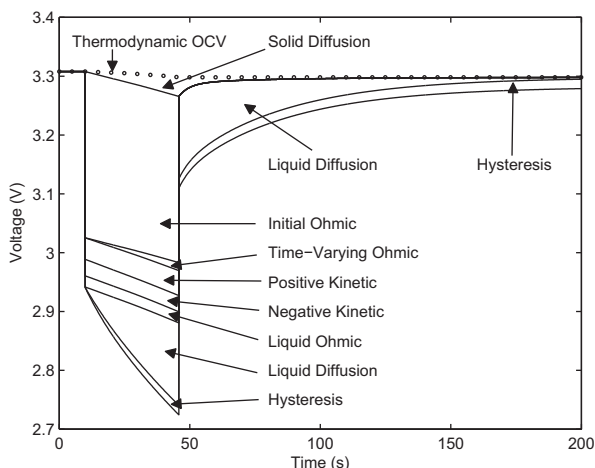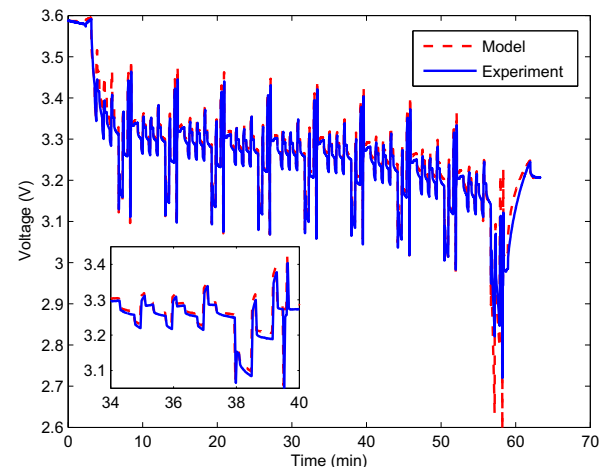

Fig. 18. Current demand and SOC trajectory for charge depleting validation.

Fig. 17. Illustration of various sources of overpotential during a 10C discharge.

Fig. 19. Model performance compared with experimental data for charge depleting operation at 55 °C.

Table 7
Summary of model error for CD operation, reported as RMS/95th percentile (mV).

Temperature	RMS/95th percentile (mV)
5 °C	96.0/220
20 °C	43.6/86.2
55 °C	19.5/42.5

than in low current portions. Additionally, the model generally overpredicts the overpotential during both discharge and charge. The most likely cause is thermal gradients within the cylindrical cell that are not as well managed due to the larger overall rate of current throughput in this case as compared to the charge sustaining case. This would lead to a warmer bulk average temperature and thus a lower overall resistance. It should also be noted that overall this current profile represents a much more dynamic situation than the CS profile so there could be additional unmodeled effects contributing to model error during the rapid transitions between discharge and charge, or vice versa. The error between the model predicted voltage and the experimental result for all tested CD conditions is summarized in Table 7.

7. Conclusions and future work

A reduced order model of Li_zC_6/Li_yFePO_4 cylindrical cells has been developed for large scale simulation, control, and estimation applications. The assumption of uniform utilization that is common for previously published reduced order models is used to develop a novel model extension incorporating the concentration and potential dynamics of the liquid phase. Both the solid and liquid phase diffusion dynamics exhibit nonlinear transfer functions that are approximated with the Pade method. This approach has the advantage of preserving the parameters of the parent model, and ultimately their physical meaning, which is useful for SOC and SOH estimation. Parameterization techniques that excite a confined portion of the overall cell dynamics are used to identify the required electrochemical parameters and their Arrhenius dependence on temperature. The parametrization procedure is validated with experimental data for a range of temperatures, SOC, and current rates, and the model proves to be robust.

Future work will apply the presented model to interpretation of capacity degradation processes during an experimental aging campaign, taking advantage of the preservation of electrochemical parameters within the reduced order structure.

Acknowledgment

References

[1] E. Karden, S. Ploumen, B. Fricke, T. Miller, K. Snyder, J. Power Sources 168 (2007) 2–11.
[2] K. Snyder, X. Yang, T. Miller, SAE Technical Paper 2009-01-1385 (2009).
[3] R. Sioshani, P. Denholm, Environ. Sci. Technol. 43 (2009) 1199–1204.
[4] Y. Hu, S. Yurkovich, Y. Guezennec, B. Yurkovich, J. Power Sources 196 (2011) 449–457.
[5] Y. Hu, S. Yurkovich, J. Power Sources 196 (2011) 2913–2923.
[6] Y. Hu, S. Yurkovich, Y. Guezennec, B. Yurkovich, Control Eng. Pract. 17 (2009) 1190–1201.
[7] G. Plett, J. Power Sources 134 (2004) 252–261.
[8] G. Plett, J. Power Sources 134 (2004) 262–276.
[9] G. Plett, J. Power Sources 134 (2004) 277–292.
[10] J. Newman, W. Tiedemann, AIChE J. 21 (1975) 25–41.
[11] M. Doyle, T. Fuller, J. Newman, J. Electrochem. Soc. 140 (1993) 1526–1533.
[12] V. Subramanian, V. Diwakar, D. Tapriyal, J. Power Sources 152 (2005) A2002–A2008.
[13] S. Santhanagopalan, Q. Guo, P. Ramadass, R. White, J. Power Sources 156 (2006) 620–628.
[14] V. Subramanian, J. Ritter, R. White, J. Electrochem. Soc. 148 (2001) E444–E449.
[15] K. Smith, C. Wang, J. Power Sources 161 (2006) 628–639.
[16] J. Forman, S. Bashash, J. Stein, H. Fathy, J. Electrochem. Soc. 158 (2011) A93–A101.
[17] L. Cai, R. White, J. Electrochem. Soc. 156 (2009) A154–A161.
[18] L. Cai, R. White, J. Electrochem. Soc. 157 (2010) A1188–A1195.
[19] S. Renganathan, R. White, J. Power Sources 196 (2011) 442–448.
[20] V. Subramanian, V. Boovaragavan, V. Ramadesigan, M. Arabandi, J. Electrochem. Soc. 156 (2009) A260–A271.
[21] V. Ramadesigan, V. Boovaragavan, J. Carl Pirkle Jr., V. Subramanian, J. Electrochem. Soc. 157 (2010) A854–A860.
[22] V. Subramanian, V. Boovaragavan, V. Diwakar, Electrochem. Solid State Lett. 10 (2007) A255–A260.
[23] P. Northrop, V. Ramadesigan, S. De, V. Diwakar, J. Electrochem. Soc. 158 (2011) A1461–A1477.
[24] V. Subramanian, D. Tapriyal, R. White, Electrochem. Solid State Lett. 7 (2004) A259–A263.
[25] K. Smith, C. Rahn, C. Wang, J. Dyn, Syst. Meas. Control 130 (2008).
[26] K. Smith, C. Rahn, C. Wang, Energy Convers. Manage. 48 (2007) 2565–2578.
[27] V. Boovaragavan, S. Haripriya, V. Subramanian, J. Power Sources 183 (2008) 361–365.
[28] K. Smith, C. Rahn, C. Wang, IEEE Trans. Control Syst. Technol. 18 (2010) 654–663.
[29] B. Haran, B. Popov, R. White, J. Electrochem. Soc. 145 (1998) 4082–4090.
[30] D. Di Domenico, G. Fiengo, A. Stefanopoulou, in: Proceedings of 2008 IEEE Conference on Control Applications, Shanghai, PR China, pp. 702–707.
[31] D. Di Domenico, G. Fiengo, A. Stefanopoulou, J. Dyn. Syst. Meas. Control – Spec. Issue. Phys. Syst. Model. 132 (2008).
[32] C. Speltino, D. Di Domenico, G. Fiengo, A. Stefanopoulou, in: Proceedings of the 2009 IEEE European Control Conference, Budapest, Hungary.
[33] S. Santhanagopalan, R. White, J. Power Sources 161 (2006) 1346–1355.
[34] A. Schmidt, M. Bitzer, A. Imre, L. Guzzella, J. Power Sources 195 (2010) 5071–5080.
[35] A. Schmidt, M. Bitzer, A. Imre, L. Guzzella, J. Power Sources 195 (2010) 7634–7638.
[36] United States Department of Energy Battery Test Manual for Plug-in Hybrid Electric Vehicles, Revision 1, INL EXT-07-12536 (2010).
[37] K. Thomas-Alyea, ECS Trans. 16 (2008) 155–165.
[38] M. Safari, C. Delacourt, J. Electrochem. Soc. 158 (2011) A63–A73.
[39] M. Safari, C. Delacourt, J. Electrochem. Soc. 158 (2011) A562–A571.
[40] M. Roscher, D. Sauer, J. Power Sources 196 (2011) 331–336.
[41] V. Srinivasan, J. Newman, J. Electrochem. Soc. 151 (2004) A1517–A1529.
[42] J. Newman, K. Thomas-Alyea, Electrochemical Systems, third ed., John Wiley and Sons, Inc., Hoboken, NJ, 2004.
[43] M. Ozisik, Boundary Value Problems of Heat Conduction, Dover Publications, Mineola, NY, 2002.
[44] M. Muratori, N. Ma, M. Canova, Y. Guezennec, in: Proceedings of the 2010 ASME Dynamic Systems and Control Conference, Boston, MA.
[45] M. Muratori, N. Ma, M. Canova, Y. Guezennec, in: Proceedings of the 2010 IFAC Symposium on Advances in Automotive Control, Munich, Germany.
[46] A. Antoulas, Approximation of Large-scale Dynamical Systems, Society for Industrial and Applied Mathematics, 2005.
[47] A.D. Filippi, S. Stockar, S. Onori, M. Canova, Y. Guezennec, in: Proceedings of the 2010 IEEE Vehicle Power and Propulsion Conference, IEEE, Lille, France.
[48] L. Juang, P. Kollmeyer, T. Jahns, R. Lorenz, in: Proceedings of the 2011 IEEE Energy Conversion Congress and Exposition, IEEE, Phoenix, AZ, pp. 2628–2634.
[49] D. Bernardi, J.-Y. Go, J. Power Sources 196 (2011) 412–427.
[50] M. Smart, J. Whitacre, B. Ratnakumar, K. Amine, J. Power Sources 168 (2007) 501–508.
[51] M. Park, X. Zhang, M. Chung, G. Less, A. Sastry, J. Power Sources 195 (2010) 7904–7929.
[52] C. Leon, J. Santamaria, M. Paris, J. Sanz, J. Ibarra, L. Torres, Phys. Rev. B 56 (1997) 5302–5305.
[53] L. Valoen, J. Reimers, J. Electrochem. Soc. 152 (2005) A882–A891.
[54] A. Rivera, J. Santamaria, C. Leon, T. Blochowicz, C. Gainaru, E. Rossler, Appl. Phys. Lett. 82 (2003) 2425–2427.
[55] S. Chung, J. Bloking, Y. Chiang, Nat. Mater. 1 (2002) 123–128.
[56] S. Bewlay, K. Konstantinov, G. Wang, S. Dou, H. Liu, Mater. Lett. 58 (2004) 1788–1791.
[57] K. Patel, J. Paulsen, J. Desilvestro, J. Power Sources 122 (2003) 144–152.